molecules

MDPI

Article

Photocatalytic Enhancement and Recyclability in Visible-Light-Responsive 2D/2D g-C_3N_4/BiOI p-n Heterojunctions via a Z-Scheme Charge Transfer Mechanism

Shuo Yang [1,2,*], Tianna Wu [1,2], Kaiyue Li [1,2], Ping Huang [1,2], Wenhui Li [1,2], Yuquan Zhuo [1,2], Keyan Liu [3], Ziwen Yang [3] and Donglai Han [3,*]

[1] School of Materials Science and Engineering, Changchun University, Changchun 130022, China; wershi98@163.com (T.W.); lkaiyue29@163.com (K.L.); huangping_2023@163.com (P.H.); 19810911969@163.com (W.L.); zyq19942867075@163.com (Y.Z.)
[2] Laboratory of Materials Design and Quantum Simulation College of Science, Changchun University, Changchun 130022, China
[3] School of Materials Science and Engineering, Changchun University of Science and Technology, Changchun 130022, China; liukeyan0910@163.com (K.L.); yzw123456789yzw@163.com (Z.Y.)
* Correspondence: yangs@ccu.edu.cn (S.Y.); dlhan_1015@cust.edu.cn (D.H.)

Abstract: With the intensification of the energy crisis and the growing concern over environmental pollution, particularly the discharge of organic dye pollutants in industrial wastewater, photocatalytic degradation of these contaminants using solar energy has emerged as an effective, eco-friendly solution. In this study, we successfully synthesized 2D/2D g-C_3N_4/BiOI p-n heterojunctions via a simple precipitation method and a high-temperature calcination method. The unique 2D structures of g-C_3N_4 nanosheets (NSs) and BiOI NSs, coupled with the synergistic effect between the two materials, significantly enhanced the photocatalytic degradation performance of the heterojunctions under simulated sunlight. The band structures, as determined by Tauc curves, Mott–Schottky curves and XPS-VB analysis, revealed a Z-scheme charge transfer mechanism that efficiently reduced charge carrier recombination and improved electron–hole separation. The photocatalytic activity of 2D/2D g-C_3N_4/BiOI p-n heterojunctions for rhodamine B (Rh B) degradation reached 99.7% efficiency within 60 min, a 2.37-fold and 1.27-fold improvement over pristine BiOI NSs and g-C_3N_4 NSs, respectively. Furthermore, the heterojunction exhibited excellent recyclability stability, with the degradation efficiency decreasing by only 1.2% after five cycles. Radical scavenging experiments confirmed the involvement of superoxide radicals ($\cdot O_2^-$) and hydroxyl radicals ($\cdot OH$) as the primary reactive species in the degradation process. This work highlights the potential of 2D/2D g-C_3N_4/BiOI p-n heterojunctions for efficient photocatalytic applications in environmental remediation.

Keywords: photocatalysis; g-C_3N_4/BiOI p-n heterojunction; efficient and recyclable; Z-scheme mechanism

check for updates

Citation: Yang, S.; T.W.; Li, K.; Huang, P.; Li, W.; Zhuo, Y.; Liu, K.; Yang, Z.; Han, D. Photocatalytic Enhancement and Recyclability in Visible-Light-Responsive 2D/2D g-C_3N_4/BiOI p-n Heterojunctions via a Z-Scheme Charge Transfer Mechanism. *Molecules* **2024**, *29*, 5418. https://doi.org/10.3390/molecules29225418

Academic Editor: Chongjun Zhao

Received: 21 October 2024
Revised: 7 November 2024
Accepted: 14 November 2024
Published: 17 November 2024

1. Introduction

With the intensification of the energy crisis and worsening environmental pollution, particularly the massive discharge of organic dye pollutants in industrial wastewater, the demand for green and renewable energy solutions has become increasingly urgent [1,2]. Photocatalytic degradation of organic pollutants in water using solar energy by semiconductor materials has emerged as an efficient, eco-friendly, and cost-effective approach to address these challenges, offering a promising alternative to traditional water treatment technologies [3,4]. In recent years, substantial efforts have been devoted to enhancing the efficiency, long-term stability, and cost-effectiveness of semiconductor photocatalysts [5]. Simultaneously, numerous semiconductor materials with visible light response characteristics have been discovered, significantly expanding the possibilities for practical photocatalytic applications [6]. Among the many visible-light-responsive semiconductors, g-C_3N_4, a two-dimensional (2D) sp^2-conjugated with carbon atoms arranged in a honeycomb lattice and a suitable band gap of 2.7 eV, has garnered increasing attention due to its easy preparation, environmental friendliness, and good thermal and chemical stability [7,8], making it a promising candidate for environmental pollution control. However, its photogenerated carrier recombination rate limits its photocatalytic efficiency, hindering its practical applications [9].

Various strategies, such as morphology control, element doping and heterojunction construction, have been explored to optimize the photocatalytic performance of g-C_3N_4 [10]. Among these methods, the construction of heterojunctions [11] is the most widely used in recent years. So far, many semiconductor materials have been reported to form heterojunction structures with g-C_3N_4, including Co_3O_4 [12], CuO [13], ZnO [14], $Bi_XO_YI_Z$ [15], Fe_2O_3 [16], and Ag_3VO_4 [17]. The construction of a 2D/2D heterostructure photocatalyst is widely regarded as an effective strategy for achieving efficient separation of photoinduced electron–hole pairs, thereby enhancing photocatalytic activity [18,19]. Zhang et al. [11] developed 2D/2D BiOBr/g-C_3N_4 heterojunctions via an in situ self-assembly method, achieving a 99% degradation efficiency of Rh B (10 $mg \cdot L^{-1}$) under simulated sunlight in only 30 min, while demonstrating excellent stability. Wang et al. [20] synthesized an ultrathin g-C_3N_4/Bi_2WO_6 composite using a bottom-up approach, achieving an impressive IBF degradation efficiency of 96% with a 25% g-C_3N_4/Bi_2WO_6 composition. BiOI, with a band gap of approximately 1.8 eV, is a good visible-light-responsive semiconductor photocatalyst featuring a unique 2D layered structure [21]. This arrangement structure can generate an internal electrostatic field, which facilitates the migration and separation of photogenerated electron–hole pairs and retains electron and hole pairs with strong redox abilities [11,14,22]. Moreover, the energy levels of BiOI can be well matched with those of g-C_3N_4, making it an ideal candidate for constructing heterojunctions. Therefore, the assembly of a 2D/2D heterojunction between 2D g-C_3N_4 and 2D BiOI could provide additional charge transfer pathways, reduce photogenerated carrier recombination and enhance carrier separation, thereby improving photocatalytic performance [23].

g-C_3N_4 can be synthesized through a variety of methods, including thermal decomposition [24,25], hydrothermal synthesis [26,27], template-assisted approaches [28], solvothermal synthesis, microwave-assisted techniques, and chemical vapor deposition. Similarly, BiOI can be prepared using methods such as hydrothermal and solvothermal synthesis, sol–gel processes, electrochemical deposition, template techniques, and microwave-assisted methods. Among these, the synthesis of g-C_3N_4 via thermal decomposition and of BiOI via the precipitation method, followed by calcinating the mix of them to form a 2D/2D g-C_3N_4/BiOI heterojunction, stands out for its simplicity, ease of implementation and cost-effectiveness, making it particularly suitable for large-scale photocatalyst production. The resulting 2D/2D g-C_3N_4/BiOI heterojunctions demonstrate significantly enhanced photocatalytic performance due to the synergistic interaction between the two materials, which effectively reduces charge carrier recombination and improves overall efficiency.

In this study, 2D/2D g-C_3N_4/BiOI p-n heterojunctions with a Z-scheme charge transfer mechanism were successfully synthesized via a precipitation method combined with a high-temperature calcination method. The synergistic effect between the two sheet-structured BiOI NSs and the g-C_3N_4 NSs significantly improves the separation of photogenerated carriers in heterojunctions, leading to a marked improvement in photocatalytic performance. The photocatalytic activities of BiOI NSs, g-C_3N_4 NSs, and 2D/2D g-C_3N_4/BiOI p-n heterojunctions were evaluated by the photocatalytic degradation of rhodamine B (Rh B) under simulated sunlight irradiation. This study focuses on the structural characteristics, recyclability stability and photocatalytic mechanism of g-C_3N_4/BiOI p-n heterojunctions, as well as the impact of the BiOI to g-C_3N_4 ratio on enhancing photocatalytic activity.

2. Results and Discussion

2.1. Structure and Morphology of BiOI, g-C_3N_4 and g-C_3N_4/BiOI

The structures and chemical bonds of BiOI NSs, g-C_3N_4 NSs, and g-C_3N_4/BiOI heterojunctions were characterized using XRD and FT-IR. Figure 1a displays the XRD patterns of the prepared BiOI NSs, g-C_3N_4 NSs, and g-C_3N_4/BiOI-(25-65) heterojunctions. Two distinct peaks of g-C_3N_4 NSs appear at approximately 13.0° and 27.5°, which align with the (100) and (002) lattice planes of g-C_3N_4 [29] (JCPDS Card No. 87-1526). The major diffraction peaks of BiOI NSs are located at around 9.7°, 29.7°, 31.7°, 45.4°, and 55.2°, corresponding to the (001), (102), (110), (200), and (212) crystal planes of the tetragonal phase BiOI [30] (JCPDS Card No. 10-0445). In the XRD image of the g-C_3N_4/BiOI heterojunctions, characteristic diffraction peaks of both tetragonal BiOI NSs and g-C_3N_4 NSs are present without any observable impurity peaks, indicating the successful synthesis of the nanocomposites. These pronounced diffraction peaks reflect the crystalline nature of the samples, allowing for an estimation of the average crystallite size using the Scherrer equation: $D = 0.9\lambda/\beta\cos\theta$,where λ is the wavelength of the X-ray radiation, β represents the full width at half maximum of the peak, and θ is the diffraction angle. The average crystallite size of samples g-C_3N_4/BiOI-(25-65) remained nearly unchanged as the amount of BiOI NSs increased in g-C_3N_4/BiOI heterojunctions, suggesting that nitrogen is not incorporated into the BiOI bulk phase but exists as a bismuth oxyhalide [31].

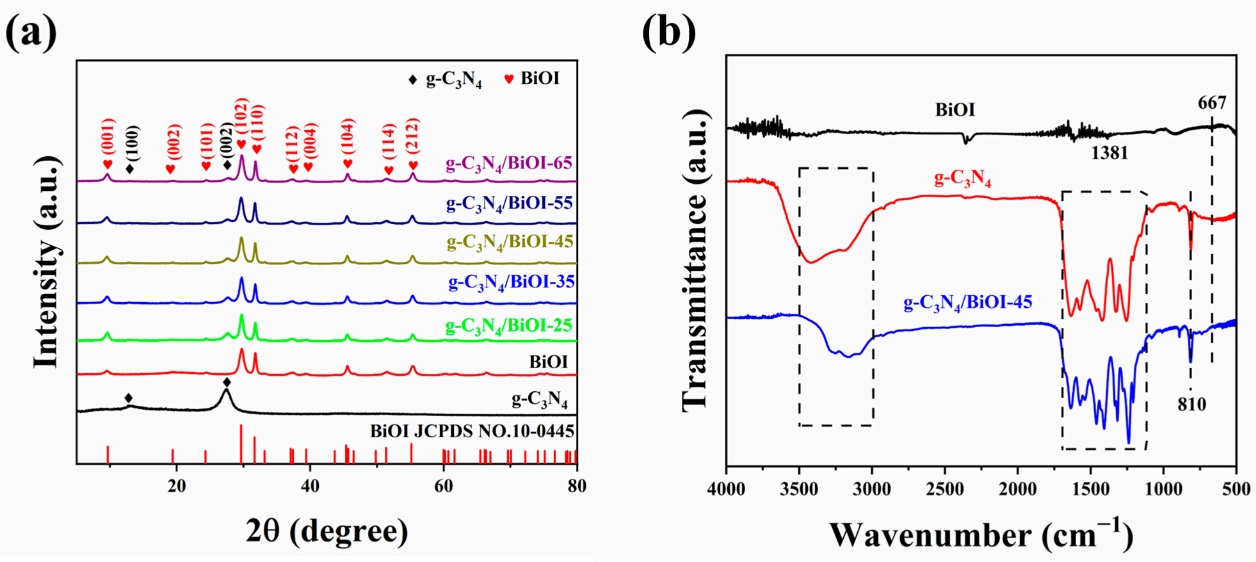

Figure 1. XRD patterns (**a**) and FT-IR spectra (**b**) of BiOI NSs, g-C_3N_4 NSs, and g-C_3N_4/BiOI heterojunctions.

Figure 1b presents the FT-IR spectra of the prepared BiOI NSs, g-C_3N_4 NSs, and g-C_3N_4/BiOI-45 heterojunctions. The FT-IR spectrum of BiOI NSs exhibits absorption peaks at 667 cm^{-1} and 1381 cm^{-1}, in accordance with the bending vibration of Bi-O bonds [32–34] and stretching vibration of I-O bonds [35,36], respectively. For g-C_3N_4 NSs, a distinct absorption peak at 810 cm^{-1} is observed, corresponding to the out-of-plane bending vibration of its heptazine ring [37,38], while peaks occurring within 1700–1200 cm^{-1} are attributed to the skeletal stretching vibrations of C-N heterocycles [39]. Additionally, broad peaks between 3500 and 3000 cm^{-1} are ascribed to the stretching vibrations of -N-H and -O-H bonds [40]. The FT-IR spectrum of the g-C_3N_4/BiOI-45 heterojunction shows no additional peaks beyond those associated with g-C_3N_4 NSs and BiOI NSs, confirming the successful preparation of the heterojunction. The absence of new peaks indicates that the two materials were combined through simple physical mixing rather than chemical bonding. However, due to the stronger intensity of the g-C_3N_4 peaks, the Bi-O bond absorption peak at 667 cm^{-1} is difficult to distinguish, necessitating further analysis via XPS, EDS, and HRTEM.

To conduct a deeper analysis of the elemental composition and chemical state of the synthesized nanocomposites, XPS was utilized. All the binding energy values are corrected by the C *1s* peak value (284.8 eV) of the indefinite carbon [41]. Figure 2a shows the XPS survey spectra of BiOI NSs, g-C_3N_4 NSs and g-C_3N_4/BiOI-45 heterojunction, confirming the presence of Bi, O, and I elements on the surface of BiOI NSs; C and N elements on the surface of g-C_3N_4 NSs; and C, N, Bi, O, and I elements on the surface of g-C_3N_4/BiOI-45 heterojunction. The observed XPS survey spectra display characteristic peaks corresponding to these elements, with no detectable impurities. Figure 2b,c present the high-resolution XPS spectra of C and N elements in g-C_3N_4 NSs and the g-C_3N_4/BiOI-45 heterojunction, while Figure 2d–f shows the high-resolution XPS spectra of Bi, O, and I elements in BiOI NSs and the g-C_3N_4/BiOI-45 heterojunction. From Figure 2b, we can see that the C *1s* spectrum of g-C_3N_4/BiOI-45 exhibits two peaks, located at 284.8 eV and 288.7 eV, where the peak at 284.8 eV is attributed to adventitious carbon used for calibration [42], and the peak at 288.7 eV corresponds to sp^2-bonded carbon in the triazine rings (N-C=N) within the aromatic structure of g-C_3N_4 [43]. In Figure 2c, the N *1s* peaks in g-C_3N_4/BiOI-45 are observed at 401.2 eV and 399.4 eV, respectively, corresponding to N-H and C-N bonds [41]. As shown in Figure 2d, the two peaks of the Bi *4f* spectrum are located at 159.0 eV and 164.3 eV, corresponding to the Bi^{3+} $4f_{7/2}$ and $4f_{5/2}$ peaks in BiOI [44–46]. In Figure 2e, the two peaks of the O 1s spectrum at 532.3 eV and 530.2 eV are consistent with oxygen vacancies and Bi-O bonds [47]. The two peaks in the I *3d* spectrum of g-C_3N_4/BiOI at 630.4 eV and 619.0 eV correspond to the I $3d_{5/2}$ and I $3d_{3/2}$ orbitals [48,49] (Figure 2f). In summary, compared to g-C_3N_4 NSs and BiOI NSs, the binding energies of C *1s*, N *1s*, Bi *4f*, O *1s*, and I *3d* in the g-C_3N_4/BiOI-45 heterojunction have shifted, confirming a successful composite reaction in the conjunction of g-C_3N_4 and BiOI. Like the C *1s* peak, the N *1s* peak in the g-C_3N_4/BiOI-45 heterojunction shifts to a higher binding energy, which can further confirm the occurrence of electron transfer between the two components.

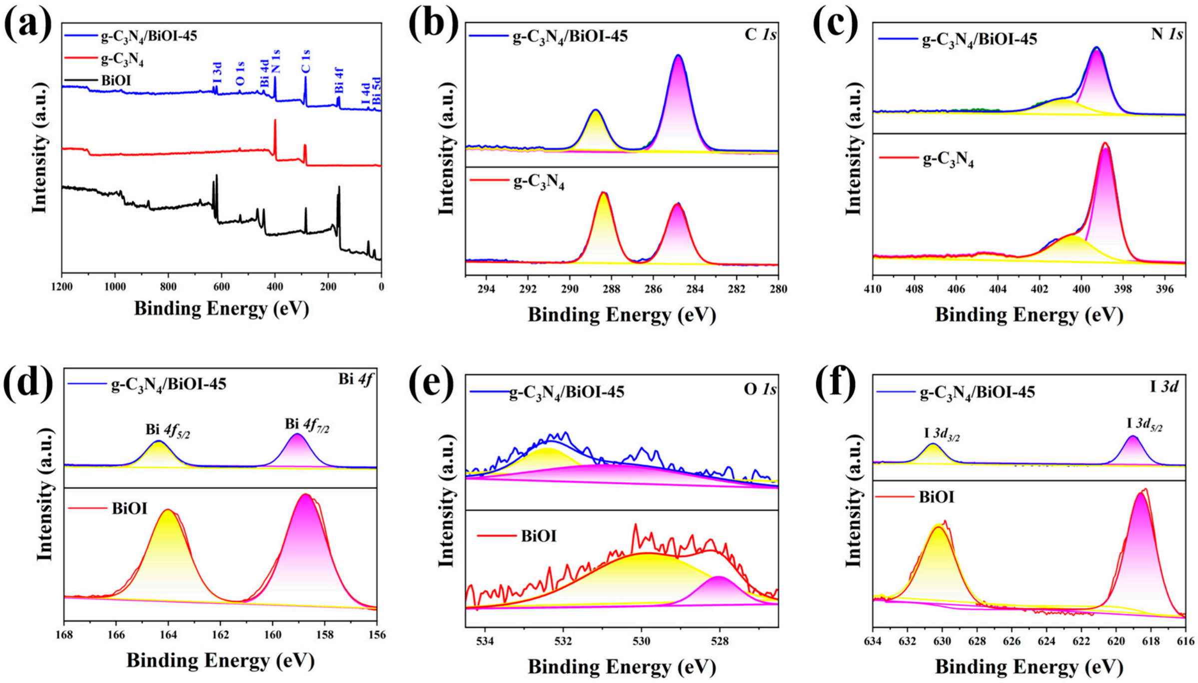

Figure 2. Full spectra (**a**); high-resolution XPS spectra of C *1s*, N *1s*, Bi *4f*, O *1s*, and I *3d* (**b**–**f**).

The prepared samples were subjected to SEM to reveal their morphology. As shown in Figure 3a, BiOI exhibits an irregular nanosheet morphology with diameters ranging from approximately 40 to 110 nm. Figure 3b reveals that g-C_3N_4 displays a smooth nanosheet with an average size of about 200–800 nm. Furthermore, Figure 3c–g displays SEM images of g-C_3N_4/BiOI nanocomposites with different mass ratios. As shown in the images, the surface of the composite becomes rougher, indicating that BiOI NSs have been successfully deposited onto the g-C_3N_4 NSs. Additionally, with an increase in the amount of deposited BiOI, the smaller BiOI NSs tend to aggregate into larger clusters. As depicted in Figure 3h–l, the C, N, Bi, O, and I elements are uniformly distributed in the g-C_3N_4/BiOI-45 samples, a finding that aligns with the XPS results.

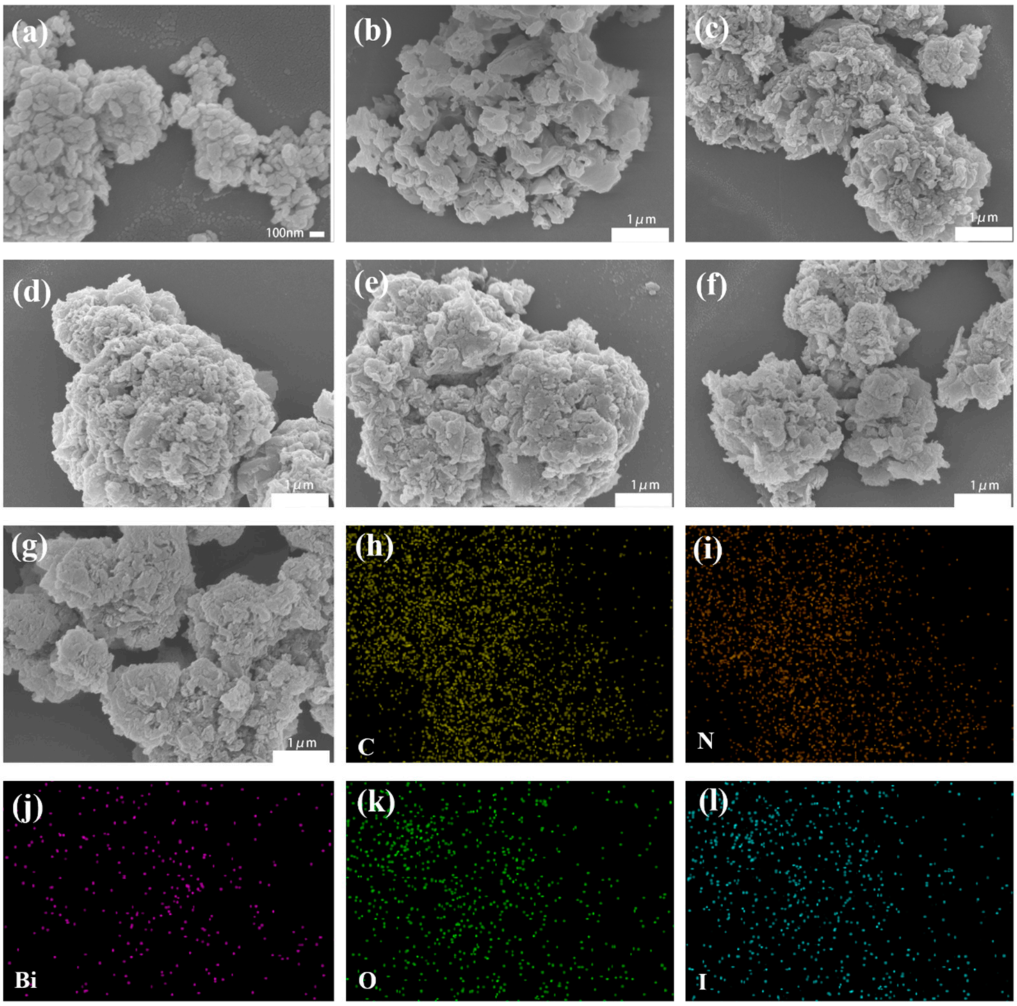

Figure 3. SEM image of BiOI NSs (**a**), g-C_3N_4 NSs (**b**), and g-C_3N_4/BiOI-(25-65) heterojunctions (**c**–**g**); EDS images of g-C_3N_4/BiOI-45 heterojunctions (**h**–**l**).

TEM and HRTEM analyses were employed to gain insights into the microstructure of BiOI NSs (Figure 4a,b) and the g-C_3N_4/BiOI-45 heterojunction (Figure 4c,d). Figure 4a clearly displays the layered nanosheet structure of BiOI, with multiple thin layers stacked together. The HRTEM image in Figure 4b reveals an interplanar spacing of approximately 0.304 nm, conforming to the lattice spacing of the tetragonal phase BiOI (102) plane [50]. Figure 4c illustrates a well-defined TEM image of g-C_3N_4/BiOI-45 heterojunctions, demonstrating the deposition of BiOI NSs on the surface of g-C_3N_4 NSs. In the HRTEM image (Figure 4d), a lattice spacing of 0.304 nm, corresponding to the (102) plane of tetragonal BiOI [50], is evident alongside the g-C_3N_4 structure. These findings are in accordance with the XRD results, confirming the successful integration of BiOI NSs and g-C_3N_4 NSs.

The specific surface area and average pore diameter of BiOI NSs, g-C_3N_4 NSs, and g-C_3N_4/BiOI heterojunctions were investigated through N_2 adsorption–desorption experiments, as shown in Figure 5. In Figure 5a, it can be observed that the BiOI, g-C_3N_4, and

g-C_3N_4/BiOI samples all exhibit Type IV adsorption isotherms with H_3 hysteresis loops. The specific surface areas of BiOI and g-C_3N_4 are 24.46 m^2/g and 54.51 m^2/g, respectively, both lower than that of g-C_3N_4/BiOI, which reaches 63.01 m^2/g. As can be seen from Figure 5b, the pore size distribution of all samples is between 10 and 30 nm, indicating their mesoporous properties. Specifically, the average pore sizes of BiOI and g-C_3N_4 are 23.52 nm and 15.93 nm, respectively, both lower than that of g-C_3N_4/BiOI heterojunctions, which have an average pore size of 24.83 nm. In summary, the g-C_3N_4/BiOI heterojunctions demonstrate increased specific surface area and mesoporous architecture, which facilitates the acquisition of additional reactive sites, thereby enhancing the photocatalytic effectiveness [51] of g-C_3N_4/BiOI heterojunctions.

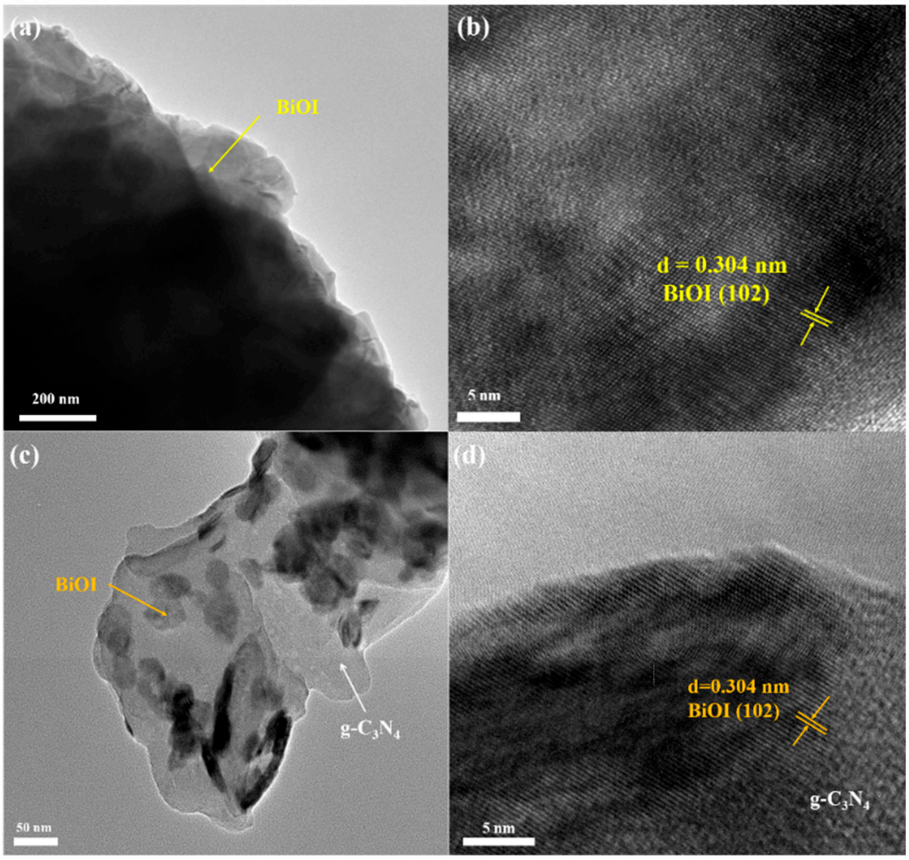

Figure 4. TEM (**a**) and HRTEM (**b**) images of BiOI NSs; TEM (**c**) and HRTEM (**d**) images of g-C_3N_4/BiOI-45 heterojunctions.

2.2. Mechanism Analysis

Figure 6a shows the UV-Vis diffuse reflectance spectra (DRS) of BiOI NSs, g-C_3N_4 NSs, and g-C_3N_4/BiOI-45 heterojunctions. The absorption edge of g-C_3N_4 NSs is at approximately 380 nm, while that of BiOI NSs is around 510 nm. The absorption edge of the g-C_3N_4/BiOI-45 heterojunction lies between those of g-C_3N_4 NSs and BiOI NSs, confirming the successful combination of the two materials. The electron–hole combination, separation, and transfer in the g-C_3N_4/BiOI-45 photocatalyst were investigated using photoluminescence (PL), photocurrent (PC) responses, and electrochemical impedance spectroscopy (EIS). As shown in Figure 6b, the PL intensity of the g-C_3N_4/BiOI-45 heterojunction is significantly lower than that of BiOI NSs and g-C_3N_4 NSs, indicating a pronounced suppression of the reassembly of photogenerated carriers after the integration of g-C_3N_4 and BiOI [52,53]. As shown in Figure 6c, the photocurrent intensity of the g-C_3N_4/BiOI-45 heterojunction is significantly higher than that of BiOI NSs and g-C_3N_4 NSs, indicating that g-C_3N_4/BiOI-45 can produce more photogenerated carriers than pure BiOI and g-C_3N_4 [51].

In parallel, as depicted in Figure 6d, the semicircle of the g-C_3N_4/BiOI-45 heterojunction is much smaller than those of BiOI NSs and g-C_3N_4 NSs, signifying a lower charge transfer resistance in the g-C_3N_4/BiOI-45 sample [54,55]. These findings suggest that the synthesized g-C_3N_4/BiOI-45 heterojunction exhibits superior photoelectrical properties and more efficient electron–hole separation and transformation.

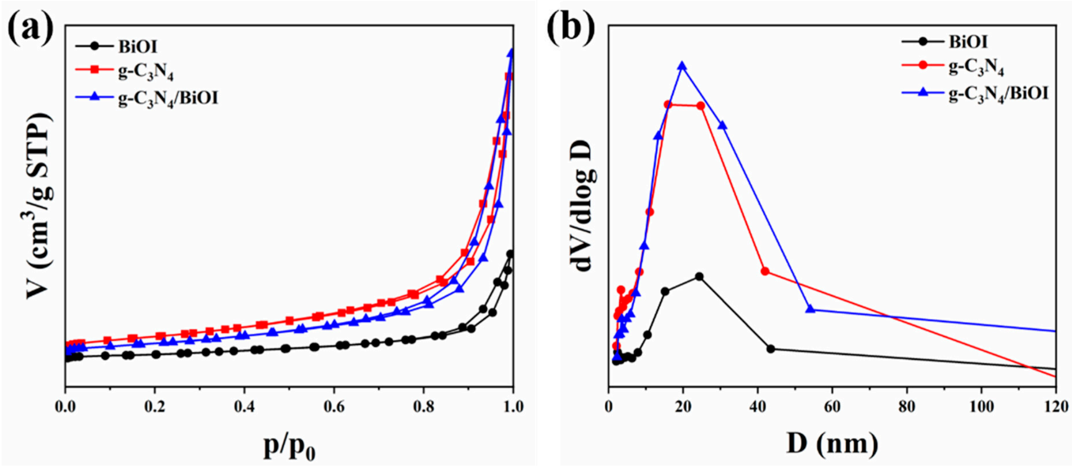

Figure 5. N_2 adsorption–desorption isotherms (**a**) and pore diameter distributions (**b**) of BiOI NSs, g-C_3N_4 NSs, and g-C_3N_4/BiOI-45 heterojunctions.

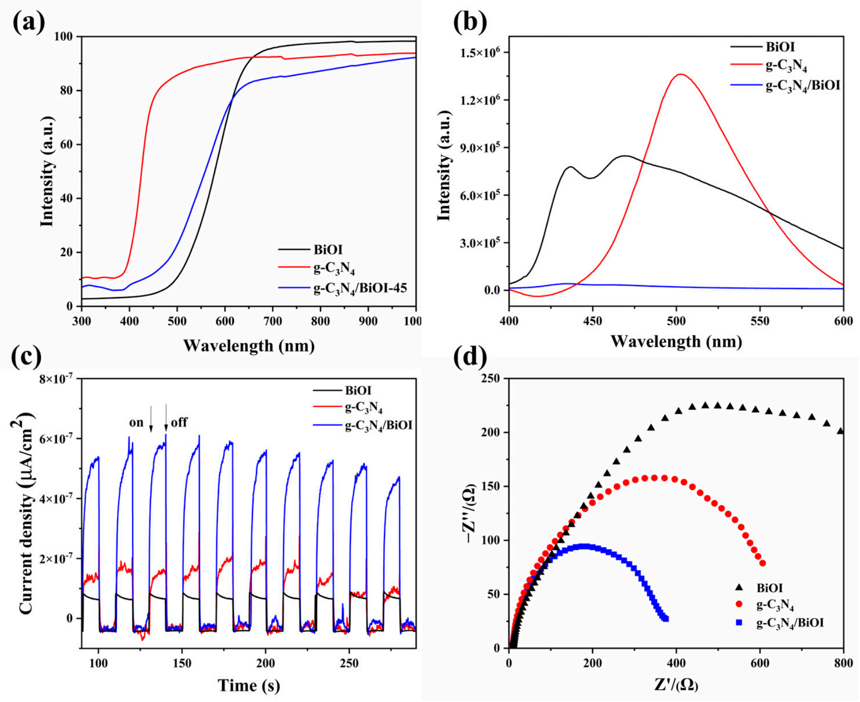

Figure 6. UV-Vis DRS (**a**), PL spectra (**b**), PC responses (**c**), and EIS Nyquist plots (**d**) of BiOI NSs, g-C_3N_4 NSs, and the g-C_3N_4/BiOI-45 heterojunction.

2.3. Photocatalytic Activity

Under simulated sunlight, we assessed the photocatalytic operation of the prepared g-C_3N_4/BiOI heterojunctions by degrading Rh B. It can be clearly seen from Figure 7a,b that, in the absence of a photocatalyst, the degradation efficiency of Rh B under simulated sunlight is extremely low, at only 2.6%, which can be considered negligible. In contrast to the individual photocatalytic performances of g-C_3N_4 NSs and BiOI NSs, the g-C_3N_4/BiOI heterojunctions show a significant improvement in photocatalytic activity towards Rh B.

Particularly, the g-C_3N_4/BiOI-45 heterojunction exhibits the best degradation efficiency, reaching 99.7% degradation within 60 min. Its photocatalytic efficiency exhibits an enhancement of 2.37-fold and 1.27-fold compared to pure BiOI NSs and g-C_3N_4 NSs, respectively. Figure 7c presents the quantitative analysis of the photocatalytic reaction kinetics using a first-order kinetic model to determine the overall reaction rate. The kinetics are described by the following equation [56]:

$$\ln{(C_t/C_0)} = -Kt \tag{1}$$

where K represents the rate constant for degradation, C_0 denotes the initial concentration of the pollutant, and C_t signifies the concentration of the pollutant at time t. Under visible light irradiation, the photocatalytic degradation kinetics of Rh B were systematically evaluated for g-C_3N_4, BiOI, g-C_3N_4/BiOI-25, g-C_3N_4/BiOI-35, g-C_3N_4/BiOI-45, g-C_3N_4/BiOI-55, and g-C_3N_4/BiOI-65. The corresponding degradation rate constants were 0.024 min^{-1}, 0.009 min^{-1}, 0.042 min^{-1}, 0.043 min^{-1}, 0.087 min^{-1}, 0.061 min^{-1}, and 0.056 min^{-1}, respectively. Notably, the g-C_3N_4/BiOI-45 heterojunction demonstrated the highest photocatalytic activity, with a degradation rate constant approximately 3.63 times that of pure g-C_3N_4 NSs and 9.67 times that of BiOI NSs. To perform additional analysis on the recyclability and stability of the g-C_3N_4/BiOI-45 heterojunction, five cycles of photocatalytic degradation measurements of Rh B were conducted (Figure 7d). With five cycles completed, the degradation efficiency decreased by only 1.2%, and the XRD pattern of the photocatalyst after cycling (Figure 7e) remained consistent with that before cycling, indicating excellent reusability and structural stability of the g-C_3N_4/BiOI-45 heterojunction.

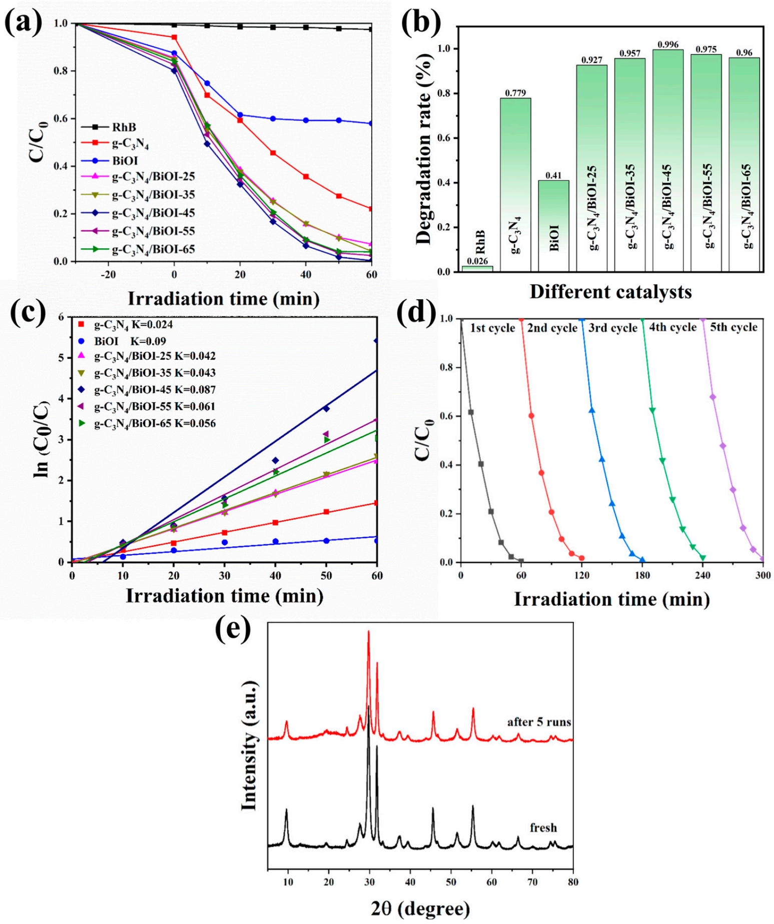

Figure 7. Photocatalytic degradation curves of Rh B under simulated sunlight irradiation (**a**) and a bar chart of the degradation rate at 60 min (**b**) for BiOI NSs, g-C_3N_4 NSs, and g-C3N4/BiOI heterojunctions; corresponding first-order kinetic curves (**c**); cycling runs of g-C_3N_4/BiOI-45 for degradation of Rh B (**d**); XRD patterns of g-C_3N_4/BiOI-45 before and after Rh B degradation cycles (**e**).

2.4. Photocatalytic Mechanism

It is well established that effective band alignment is crucial for achieving high photocatalytic performance in heterojunction photocatalysts. To determine the band positions of the g-C_3N_4 NSs and BiOI NSs, Tauc plots, Mott–Schottky (M-S) curves, and XPS valence band (XPS-VB) spectra were employed to estimate the flat band potentials (Fermi energy level, E_f), valence band maximum (VBM), and conduction band minimum (CBM). As shown in Figure 8a, the Tauc formula is given by:

$$\alpha h v = K\left(h v - E_g\right)^{\frac{1}{2}} \tag{2}$$

where K represents the parameter related to material properties, h is the Planck constant, α signifies the absorption coefficient, and v is the frequency of the incident photons [57]. From Figure 8a, the bandgap energies (E_g) of BiOI NSs and g-C_3N_4 NSs were derived to be 2.02 eV and 2.83 eV, respectively. Based on the M-S curves, the E_f of BiOI NSs and g-C_3N_4 NSs were found to be 0.68 eV and −0.45 eV (vs. Ag/AgCl), respectively. The positive slope of the M-S curve indicates that g-C_3N_4 is an n-type semiconductor, while the negative slope for BiOI confirms it as a p-type semiconductor. These values were then converted to the standard hydrogen electrode (NHE) potential using the following equation [58]:

$$E_{NHE} = E_{Ag/AgCl} + 0.198\ V \tag{3}$$

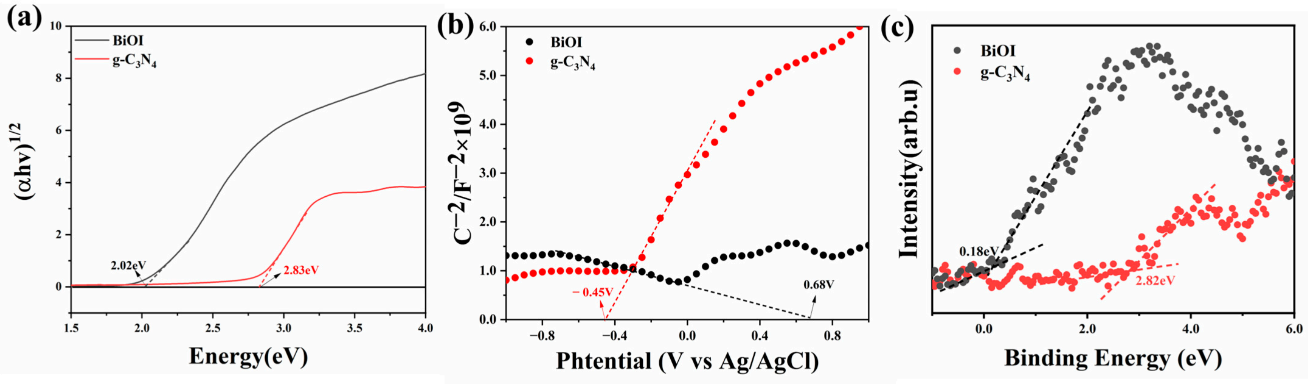

Figure 8. Tauc curves (**a**), Mott–Schottky curves (**b**), and VB-XPS spectra (**c**) of BiOI NSs and g-C_3N_4 NSs.

Therefore, the E_f values of BiOI NSs and g-C_3N_4 NSs under NHE conditions were calculated as 0.88 V and −0.25 V, respectively. The relative potential values of VBM to E_f for BiOI NSs and g-C_3N_4 NSs were estimated using VB-XPS spectra (Figure 8c) and found to be 0.18 eV and 2.82 eV, respectively. In accordance with the E_f values and VB-XPS results, the E_{VB} values of BiOI NSs and g-C_3N_4 NSs were evaluated to be 1.06 V and 2.57 V vs. NHE, respectively. Subsequently, utilizing the following formula [59]:

$$E_g = E_{VB} - E_{CB} \tag{4}$$

The E_{CB} values of BiOI NSs and g-C_3N_4 NSs were estimated to be −0.96 V and −0.26 V, respectively.

Based on these band structure data, we plotted two possible mechanisms in the application of photocatalytic degradation of Rh B by g-C_3N_4/BiOI-45 p-n heterojunctions: the dual charge transfer mechanism and Z-scheme transfer mechanism. As illustrated in Figure 9(a1), under simulated sunlight irradiation, both BiOI NSs and g-C_3N_4 NSs are excited simultaneously, generating photogenerated electrons (e^-) that transition from the VBM to the CBM, leaving holes (h^+) in their respective VBMs. Subsequently, the e^- in the CBM of BiOI NSs migrates to the CBM of g-C_3N_4 NSs, while the h^+ in the VBM of g-C_3N_4 NSs transfers to the VBM of BiOI NSs. This results in the e^- remaining in the CBM of

$g\text{-}C_3N_4$ NSs with an energy level of −0.28 V, which is higher than the $O_2/\cdot O_2^-$ potential (−0.33 V vs. NHE [41,48]). Consequently, the e^- in the CBM of $g\text{-}C_3N_4$ NSs cannot reduce O_2 to $\cdot O_2^-$. Similarly, h^+ remain in the VBM of BiOI NSs with an energy level of 0.14 V, which is lower than the $\cdot OH/H_2O$ potential (2.4 V vs. NHE [48]), preventing the h^+ in the VBM of BiOI NSs from oxidizing H_2O to produce $\cdot OH$. Therefore, under this dual charge transfer mechanism, the only active species in the photocatalysts should be h^+. In contrast, the potential double Z-scheme transfer mechanism, as depicted in Figure 9(a2), suggests that e^- in the CBM of $g\text{-}C_3N_4$ NSs recombine with h^+ in the VBM of BiOI NSs, forming a built-in electric field at the interface, which prevents further recombination of electrons and holes. Subsequently, e^- remain in the CBM of BiOI NSs at an energy level of −1.88 V, which is lower than the $O_2/\cdot O_2^-$ potential, allowing the electrons in the CBM of BiOI NSs to react with O_2 to generate $\cdot O_2^-$. Simultaneously, h^+ remain in the VBM of $g\text{-}C_3N_4$ NSs with an energy level of 2.53 V, which is higher than the $\cdot OH/H_2O$ potential, enabling the h^+ in the VBM of $g\text{-}C_3N_4$ NSs to react with H_2O to produce $\cdot OH$. Under the Z-scheme electron transfer mechanism, the active species $\cdot O_2^-$, $\cdot OH$, and h^+ can all react with pollutants, decomposing them into H_2O and CO_2.

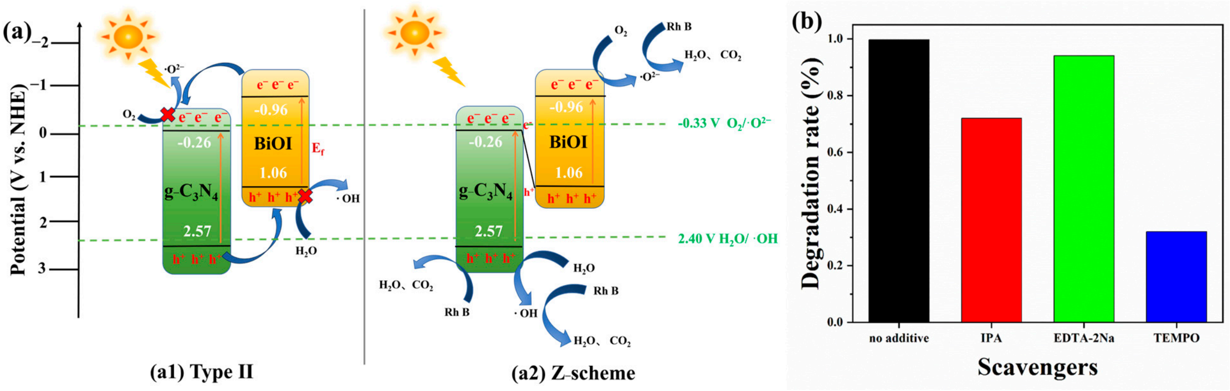

Figure 9. Schematic illustration of the photodegradation process (**a**) and radical scavenging experiments (**b**) for Rh B degradation under simulated sunlight using the $g\text{-}C_3N_4$/BiOI p-n heterojunctions.

To confirm the photocatalytic mechanism, radical scavenging experiments were performed. The procedure followed the same steps as the photocatalytic experiments, with the addition of specific scavengers (1 mmol/L) to the degradation solution. IPA, EDTA-2Na, and TEMPO were used to selectively capture hydroxyl radicals ($\cdot OH$), holes (h^+), and superoxide radicals ($\cdot O_2^-$), respectively. As shown in Figure 9b, upon the addition of EDTA-2Na, the photocatalytic degradation efficiency of $g\text{-}C_3N_4$/BiOI-45 p-n heterojunctions for Rh B decreased from 99.7% to 94.1%, indicating the involvement of h^+ as an active species in the photocatalytic process, albeit with a relatively minor impact. After the introduction of IPA, the degradation efficiency dropped to 72.0% suggesting that $\cdot OH$ also contributes to photocatalytic degradation. When TEMPO was added, the photocatalytic degradation efficiency further decreased to 32.0%, confirming that $\cdot O_2^-$ plays the most significant role and is the primary active species. These results indicate that $\cdot O_2^-$ and $\cdot OH$ are the dominant reactive intermediates, while h^+ plays a less significant role in the degradation of Rh B. This observation aligns with our proposed Z-scheme transfer mechanism.

In recent years, researchers have made significant efforts in developing a wide range of photocatalysts, such as $Bi_4Ti_3O_{12}/AgI$ [60], $Ag_2CrO_4/g\text{-}C_3N_4$ [61], $Bi_2MoO_6/Bi_2Mo_3O_{12}$ [62], $BiVO_4/g\text{-}C_3N_4$ [63], $Cu_2O/BiOBr$ [64], etc., to enhance the degradation performance of Rh B. As shown in Table 1, it is evident that even when the components of the heterojunction photocatalysts are identical, the photocatalytic degradation efficiency varies due to different experimental conditions, such as the amount of catalyst used, the concentration of Rh B, the light source employed in photocatalytic degradation experiments, the distance between the sample and the light source, and the exposure time. Consequently, the degradation efficiency of Rh B also differs when different photocatalysts or experimental conditions are used.

Table 1. List of diverse photocatalysts studied for degrading Rh B.

Sample	Amount	Application	Concentration and Usage	Power Source	Time	Efficiency	Ref.
$Bi_4Ti_3O_{12}$/AgI heterojunction	20 mg	Rh B degradation	20 mg/L 60 mL	–	60 min	92.5%	Liu et al. [60]
Ag_2CrO_4/g-C_3N_4heterojunction	50 mg	Rh B degradation	2×10^{-5} M 100 mL	Xe lamp 300 W	120 min	94%	Alsalme et al. [61]
Bi_2MoO_6/$Bi_2Mo_3O_{12}$ heterojunction	30 mg	Rh B degradation	10 mg/L 30 mL	Xe lamp 300 W	30 min	95%	Wang et al. [62]
$BiVO_4$/g-C_3N_4 heterojunction	180 mg	Rh B degradation	10 mg/L 180 mL	Xe lamp 500 W	75 min	98%	Khan et al. [63]
Cu_2O/BiOBr heterojunction	50 mg	Rh B degradation	100 mg/L 100 mL	Xe lamp 300 W	50 min	82.33%	Gao et al. [64]
β-Bi_2O_3/TiO_2 heterojunction	50 mg	Rh B degradation	20 mg/L 60 mL	Xe lamp 300 W	60 min	99.6%	Wang et al. [65]
MoS_2/ZnO heterojunction	25 mg	Rh B degradation	10 mg/L 50 ml	Xe lamp 200 W	50 min	95%	Gang et al. [66]
$ZnIn_2S_4$/Bi_2WO_6 heterojunction	10 mg	Rh B degradation	10 mg/L 50 mL	Xe lamp 300 W	40 min	93.49	Liu et al. [67]
BiOI/$AgEuW_2O_8$ heterojunction	60 mg	Rh B degradation	30 mg/L 100 mL	Xe lamp 300 W	180 min	91.77%	Wu et al. [68]
CuO/MoO_3 heterojunction	15 mg	Rh B degradation	8 mg/L 60 mL	Xe lamp 400 W	120 min	99%	Hussain et al. [69]
BiOBr/CdS heterojunction	20 mg	Rh B degradation	10 mg/L 40 mL	LED light 5 W	60 min	97%	Yu et al. [70]
SnO_2/g-C_3N_4 composite	100 mg	Rh B degradation	30 mg/L 200 mL	LED light 30 W	150 min	99.42%	Van et al. [71]
$CuWO_4$/CuS heterojunction	40 mg	Rh B degradation	15 mg/L 100 mL	Xe lamp 300 W	90 min	93.2%	Cui et al. [72]
CuO/g-C_3N_4 heterojunction	100 mg	Rh B degradation	5 mg/L 100 mL	Xe lamp 300 W	30 min	88.9%	Zhu et al. [73]

3. Experiment

3.1. Experimental Materials

Pentahydrate bismuth nitrate ($Bi(NO_3)_3 \cdot 5H_2O$, AR, 99.0%) was purchased from Shanghai Macklin Biochemical Technology Co., Ltd., Shanghai, China, while potassium iodide (KI, AR, $\geq$99.0%), mannitol ($C_6H_{14}O_6$, AR, 98.0%), urea ($CO(NH_2)_2$, $\geq$99.5%), rhodamine B (Rh B, AR), 4-hydroxy-TEMPO (TEMPO, 98%), Isopropyl alcohol (IPA, AR, $\geq$99.5%), and ethylenediaminetetraacetic acid disodium salt (EDTA-2Na, 0.1000 mol/L (0.1 M)) were all acquired from Shanghai Aladdin Biochemical Technology Co., Ltd., Shanghai, China. All chemicals were employed without further purification.

3.2. Preparation of Heterojunction Materials

3.2.1. Preparation of g-C_3N_4 NSs

To begin, we weighed a specific amount of $CO(NH_2)_2$ and placed it into a crucible, then heated it in a muffle furnace at a rate of 5 °C per minute until the temperature reached 550 °C; we subsequently calcined it for 2 h and then cooled it to room temperature. The resulting light-yellow solid was immersed in a nitric acid solution with a pH of 1 and stirred at 60 °C for 8 h. After washing several times with deionized water, the material was subjected to drying at 80 °C for 3 h. The dried product was then returned to the muffle furnace, where the temperature was raised at a rate of 5 °C per minute to 500 °C and calcined for another 2 h before cooling. This process yielded g-C_3N_4 NSs.

3.2.2. Preparation of BiOI NSs

We dissolved 2.425 g of $Bi(NO_3)_3 \cdot 5H_2O$ in 60 mL of deionized water and stirred it magnetically for 1 h. Simultaneously, we dissolved 5.0 mmol of KI in 40 mL of deionized water under magnetic stirring for 1 h. Subsequently, 0.25 g of $C_6H_{14}O_6$ was added to the solution containing $Bi(NO_3)_3 \cdot 5H_2O$, and it continued to stir for 30 min. Then, the KI solution was slowly poured along the inner wall of the beaker into the $Bi(NO_3)_3 \cdot 5H_2O$ solution. It was then stirred continuously at 60 °C for 3 h. The resulting BiOI nanomaterials were washed several times with deionized water and anhydrous ethanol, followed by vacuum drying at 60 °C for 12 h to obtain the BiOI NSs.

3.2.3. Preparation of g-C_3N_4/BiOI heterojunctions

To prepare the heterojunctions, 0.1 g of g-C_3N_4 and 0.045 g of BiOI NSs were separately weighed. Subsequently, they were mixed with anhydrous ethanol and ground together until the ethanol evaporated completely. The resulting orange product was then transferred into a crucible and heated in a muffle furnace at a rate of 5 °C per minute up to 300 °C. The sample was calcined for 2 h and then cooled to obtain the g-C_3N_4/BiOI nanocomposites. The detailed synthesis procedure is described in Scheme 1. Different amounts of BiOI photocatalysts were added during the reaction process, and the corresponding mass ratios are detailed in Table 2.

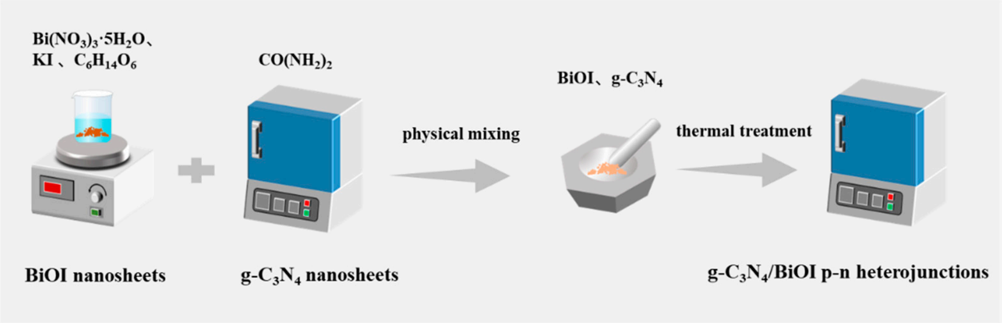

Scheme 1. Synthesis process of g-C_3N_4/BiOI heterojunctions.

Table 2. Composition ratios of g-C_3N_4 and BiOI and the corresponding nomenclature for g-C_3N_4/BiOI samples.

g-C_3N_4 (mg)	BiOI (mg)	Symbols of g-C_3N_4/BiOI
100	25	g-C_3N_4/BiOI-25
100	35	g-C_3N_4/BiOI-35
100	45	g-C_3N_4/BiOI-45
100	55	g-C_3N_4/BiOI-55
100	65	g-C_3N_4/BiOI-65

3.3. Characterization of Materials

X-ray diffraction (XRD) patterns were recorded using a Bruker D2 Phaser X-ray diffractometer, manufactured by Bruker AXS GmbH, located in Karlsruhe, Germany. The system was operated at 30 kV with Cu Kα radiation (λ = 1.5406 Å), a current of 10 mA, and a step size of 0.02°, scanning in the range of 5 to 80 degrees. The software version used for data acquisition was DIFFRAC.MEASUREMENT CENTER V7. X-ray photoelectron spectroscopy (XPS) was performed with a Thermo Fisher Scientific ESCALAB 250Xi system, manufactured by Thermo Fisher Scientific Inc., located in Waltham, MA, USA. The morphological characteristics of the prepared nanomaterials were analyzed using a Tecnai F20 transmission electron microscope (TEM) operated at 200 kV and a JSM-6701F scanning electron microscope (SEM) operated at 10 kV. UV-Vis diffuse reflectance spectra (UV-Vis DRS) in the range of 200–800 nm and UV-Vis absorption spectra in the range of 200–700 cm^{-1} were collected using a SHIMADZU UV-3600 Plus spectrophotometer, manufactured by Shimadzu Scientific Instruments (SSI), headquartered in Columbia, MD, USA. Surface area and pore size distribution of the samples were measured using a JW-BK200C analyzer (Beijing JWGB Sci & Tech Co., Ltd, Beijing, China) under a nitrogen atmosphere. Fourier transform infrared (FT-IR) spectra were obtained using a SHIMADZU IRTracer-100 spectrophotometer, manufactured by Shimadzu Scientific Instruments (SSI), headquartered in Columbia, MD, USA. Samples were thoroughly mixed with KBr and pressed into pellets. Photoluminescence (PL) spectra were acquired using a Hitachi F-4700 fluorescence spectrophotometer at room temperature with an excitation wavelength of 325 nm. In this electrochemical impedance spectroscopy (EIS) experiment, the potential was set at 0.1 V with an amplitude of 0.005 V using a 0.5 M Na_2SO_4 solution across a frequency range of 0.01 to 10 kHz.

3.4. Photocatalytic Degradation Experiment

During the photocatalytic process, the absorbance (A) of the analyte at different time intervals was measured using the UV-3600 Plus spectrophotometer. According to Lambert–Beer's law, the A was proportional to the concentration of the target contaminant (C). The photocatalytic degradation efficiency (D) was calculated by Equation (5) as follows [74]:

$$D = \frac{C_0 - C_t}{C_0} \times 100\% = \frac{A_0 - A_t}{A_0} \times 100\% \quad (5)$$

where C_0 denotes the initial concentration of the target pollutant (mg/L), C_t indicates the concentration of the target pollutant at time t during the photocatalytic process (mg/L), A_0 stands for the initial absorbance values of the target pollutant, and A_t stands for its absorbance values at time t during the photocatalytic process. The specific operation of the photocatalytic degradation experiment is as follows: using a Microsolar 300 photocatalytic device (Beijing Perfectlight Technology Co., Ltd., Beijing, China) as the reaction device to simulate sunlight, 10 mg of photocatalyst was poured into a beaker containing 10 mg/L of dye solution. To exclude the influence of the photocatalytic degradation efficiency by the adsorption of the catalyst and the effect of dye sensitization, the dye–photocatalyst mixture was placed in a dark room for 30 min to achieve adsorption–desorption equilibrium. Subsequently, the power was turned on, and the beaker was positioned 15 cm away from the light source. The variation in the Rh B absorption peak at 553 nm was recorded at 10-minute intervals to determine the contaminant concentrations during photocatalytic degradation. The photocatalytic time and photocatalytic conditions of the repeatability experiment were not changed. After each photocatalytic cycle, the photocatalyst was ultrasonically washed several times with absolute ethanol. Since the catalyst may be reduced during each wash, an analytical balance was used to weigh the photocatalyst and measure the degradation solution in the same ratio before proceeding to the next photocatalytic test. The operation was repeated 5 times to complete the repeatability test.

4. Conclusions

To summarize, we successfully prepared mesoporous 2D/2D g-C_3N_4/BiOI p-n heterojunctions through a combination of the precipitation method and high-temperature calcination. Compared to pure g-C_3N_4 NSs and BiOI NSs, the g-C_3N_4/BiOI p-n heterojunctions exhibited lower electron–hole pair recombination rates, increased photogenerated electrons, and smaller charge transfer resistances, resulting in significantly higher photocatalytic activity. Under simulated sunlight, the g-C_3N_4/BiOI heterojunction achieved a 99.7% degradation efficiency of Rh B within 60 min, representing an increase of 2.37 and 1.27 times over pure BiOI NSs and g-C_3N_4 NSs, respectively. The electron transfer mechanism in the g-C_3N_4/BiOI-45 p-n heterojunction followed a Z-mechanism, which was further validated by radical scavenging experiments. These experiments confirmed that $\cdot O_2^-$ and $\cdot OH$ are the main reactive species responsible for the degradation process. Additionally, the degradation efficiency of the g-C_3N_4/BiOI-45 heterojunction decreased by only 1.2% after five cycles, and the XRD diffraction peaks remained unchanged, demonstrating the material's excellent recyclability and stability. This study not only demonstrates the enhanced photocatalytic potential of 2D/2D heterojunctions but also provides an effective and low-cost method for their large-scale production, making them promising candidates for addressing environmental pollution issues.

Author Contributions: Conceptualization, S.Y.; methodology, T.W.; validation, K.L. (Kaiyue Li) and P.H.; formal analysis, T.W. and S.Y.; investigation, S.Y.; resources, S.Y.; data curation, T.W.; writing—original draft preparation, T.W.; writing—review and editing, D.H.; visualization, P.H., W.L., K.L. (Keyan Liu), Y.Z. and Z.Y.; funding acquisition, Han, D. All authors have read and agreed to the published version of the manuscript.

Funding: This research was funded by the Program of the Jilin Provincial Science and Technology Development Project and the grant number is YDZJ202401541ZYTS.

Institutional Review Board Statement: Not applicable.

Informed Consent Statement: Not applicable.

Data Availability Statement: Data are contained within the article.

Conflicts of Interest: The authors declare no conflict of interest.

References

1. Theerthagiri, J.; Karuppasamy, K.; Lee, S.J.; Shwetharani, R.; Kim, H.-S.; Pasha, S.K.K.; Ashokkumar, M.; Choi, M.Y. Fundamentals and comprehensive insights on pulsed laser synthesis of advanced materials for diverse photo- and electrocatalytic applications. *Light Sci. Appl.* **2022**, *11*, 250. [CrossRef] [PubMed]
2. Fan, Y.; Huang, W.; Zhu, F.; Liu, X.; Jin, C.; Guo, C.; An, Y.; Kivshar, Y.; Qiu, C.-W.; Li, W. Dispersion-assisted high-dimensional photodetector. *Nature* **2024**, *630*, 77–83. [CrossRef] [PubMed]
3. Du, K.; Feng, J.; Gao, X.; Zhang, H. Nanocomposites based on lanthanide-doped upconversion nanoparticles: Diverse designs and applications. *Light Sci. Appl.* **2022**, *11*, 222. [CrossRef] [PubMed]
4. Zhao, Z. Research progress of semiconductor photocatalysis applied to environmental governance. *IOP Conf. Ser. Earth Environ. Sci.* **2021**, *631*, 012022. [CrossRef]
5. Karthikeyan, C.; Arunachalam, P.; Ramachandran, K.; Al-Mayouf, A.M.; Karuppuchamy, S. Recent advances in semiconductor metal oxides with enhanced methods for solar photocatalytic applications. *J. Alloys Compd.* **2020**, *828*, 154281. [CrossRef]
6. Ahmad, I.; Zou, Y.; Yan, J.; Liu, Y.; Shukrullah, S.; Naz, M.Y.; Hussain, H.; Khan, W.Q.; Khalid, N.R. Semiconductor photocatalysts: A critical review highlighting the various strategies to boost the photocatalytic performances for diverse applications. *Adv. Colloid Interface Sci.* **2022**, *311*, 102830. [CrossRef]
7. Iqbal, W.; Dong, C.; Xing, M.; Tan, X.; Zhang, J. Eco-friendly one-pot synthesis of well-adorned mesoporous g-C_3N_4 with efficiently enhanced visible light photocatalytic activity†. *Catal. Sci. Technol.* **2017**, *7*, 1726–1734. [CrossRef]
8. Zhang, B.; Hu, X.; Liu, E.; Fan, J. Novel S-scheme 2D/2D BiOBr/g-C_3N_4 heterojunctions with enhanced photocatalytic activity. *Chin. J. Catal.* **2021**, *42*, 1519–1529. [CrossRef]
9. Luo, W.; Chen, X.; Wei, Z.; Liu, D.; Yao, W.; Zhu, Y. Three-dimensional network structure assembled by g-C_3N_4 nanorods for improving visible-light photocatalytic performance. *Appl. Catal. B Environ. Energy* **2019**, *255*, 117761. [CrossRef]
10. He, F.; Wang, Z.; Li, Y.; Peng, S.; Liu, B. The nonmetal modulation of composition and morphology of g-C_3N_4-based photocatalysts. *Appl. Catal. B Environ. Energy* **2020**, *269*, 118828. [CrossRef]
11. Shahzad, R.; Muneer, M.; Khalid, R.; Amin, H.M.A. ZnO-Bi_2O_3 Heterostructured Composite for the Photocatalytic Degradation of Orange 16 Reactive Dye: Synergistic Effect of UV Irradiation and Hydrogen Peroxide. *Catalysts* **2023**, *13*, 1328. [CrossRef]
12. Fan, L.; Wang, Z.; Wang, Y.; Ai, H.; Zhang, W.; Liu, X.; Han, X.; Zhao, J.; Zhang, H. Exploiting synergistic effects: Co_3O_4/g-C_3N_4 composite catalyst for enhanced oxygen evolution reaction. *Int. J. Electrochem. Sci.* **2023**, *18*, 100394. [CrossRef]
13. Kavil, J.; Anjana, P.M.; Joshy, D.; Babu, A.; Raj, G.; Periyat, P.; Rakhi, R.B. g-C_3N_4/CuO and g-C_3N_4/Co_3O_4 nanohybrid structures as efficient electrode materials in symmetric supercapacitors. *RSC Adv.* **2019**, *9*, 38430–38437. [CrossRef] [PubMed]
14. Kalaiarasan, S.; Shanthi, C. Synthesis and characterization of G-C_3N_4@ZnO photo catalyst on removal of toxic pollutants. *J. Ovonic Res.* **2022**, *18*, 219–226. [CrossRef]
15. Huang, H.; Liu, C.; Ou, H.; Ma, T.; Zhang, Y. Self-sacrifice transformation for fabrication of type-I and type-II heterojunctions in hierarchical BixOyIz/g-C_3N_4 for efficient visible-light photocatalysis. *Appl. Surf. Sci.* **2019**, *470*, 1101–1110. [CrossRef]
16. Wei, L.; Zhang, X.; Wang, J.; Yang, J.; Yang, X. Synthesis of Fe_2O_3/g-C_3N_4 composite with efficient photocatalytic degradation for methyl orange. *Inorg. Chem. Commun.* **2023**, *159*, 111890. [CrossRef]
17. Wang, S.; Li, D.; Sun, C.; Yang, S.; Guan, Y.; He, H. Synthesis and characterization of g-C_3N_4/Ag_3VO_4 composites with significantly enhanced visible-light photocatalytic activity for triphenylmethane dye degradation. *Appl. Catal. B Environ. Energy* **2014**, *144*, 885–892. [CrossRef]
18. Wang, K.; Li, Y.; Li, J.; Zhang, G. Boosting interfacial charge separation of $Ba_5Nb_4O_{15}$/g-C_3N_4 photocatalysts by 2D/2D nanojunction towards efficient visible-light driven H_2 generation. *Appl. Catal. B Environ. Energy* **2020**, *263*, 117730. [CrossRef]

19. Lu, M.; Li, Q.; Zhang, C.; Fan, X.; Li, L.; Dong, Y.; Chen, G.; Shi, H.J.C. Remarkable photocatalytic activity enhancement of CO_2 conversion over 2D/2D g-C_3N_4/$BiVO_4$ Z-scheme heterojunction promoted by efficient interfacial charge transfer. *Carbon* **2020**, *160*, 342–352. [CrossRef]
20. Wang, J.; Tang, L.; Zeng, G.; Deng, Y.; Liu, Y.; Wang, L.; Zhou, Y.; Guo, Z.; Wang, J.; Zhang, C. Atomic scale g-C_3N_4/Bi_2WO_6 2D/2D heterojunction with enhanced photocatalytic degradation of ibuprofen under visible light irradiation. *Appl. Catal. B Environ. Energy* **2017**, *209*, 285–294. [CrossRef]
21. Ekthammathat, N.; Kidarn, S.; Phuruangrat, A.; Thongtem, S.; Thongtem, T. Hydrothermal synthesis of Ag-doped BiOI nanostructure used for photocatalysis. *Res. Chem. Intermed.* **2015**, *42*, 5559–5572. [CrossRef]
22. Wang, T.; Zhao, C.; Meng, L.; Li, Y.; Chu, H.; Wang, F.; Tao, Y.; Liu, W.; Wang, C.-C. In-situ-construction of BiOI/UiO-66 heterostructure via nanoplate-on-octahedron: A novel p-n heterojunction photocatalyst for efficient sulfadiazine elimination. *Chem. Eng. J.* **2022**, *451*, 138624. [CrossRef]
23. Dai, W.-W.; Zhao, Z.-Y. Understanding the interfacial properties of graphene-based materials/BiOI heterostructures by DFT calculations. *Appl. Surf. Sci.* **2017**, *406*, 8–20. [CrossRef]
24. Pérez-Molina, Á.; Pastrana-Martínez, L.M.; Pérez-Poyatos, L.T.; Morales-Torres, S.; Maldonado-Hódar, F.J. One-Pot Thermal Synthesis of g-C_3N_4/ZnO Composites for the Degradation of 5-Fluoruracil Cytostatic Drug under UV-LED Irradiation. *Nanomaterials* **2022**, *12*, 340. [CrossRef]
25. Wang, X.; Maeda, K.; Thomas, A.; Takanabe, K.; Xin, G.; Carlsson, J.M.; Domen, K.; Antonietti, M. A metal-free polymeric photocatalyst for hydrogen production from water under visible light. *Nat. Mater.* **2008**, *8*, 76–80. [CrossRef]
26. Vijayakumar, T.P.; Benoy, M.D.; Duraimurugan, J.; Kumar, G.S.; Mohd, S.; Maadeswaran, P.; Kumar, A.S.; Kumar, K.A.R. Hydrothermal synthesis of CuO/g-C_3N_4 nanosheets for visible-light driven photodegradation of methylene blue. *Diam. Relat. Mater.* **2021**, *121*, 108735. [CrossRef]
27. Zhang, G.; Zhang, J.; Zhang, M.; Wang, X. Polycondensation of thiourea into carbon nitride semiconductors as visible light photocatalysts. *J. Mater. Chem.* **2012**, *22*, 8083–8091. [CrossRef]
28. Huang, H.; Jiang, L.; Yang, J.; Zhou, S.; Yuan, X.; Liang, J.; Wang, H.; Wang, H.; Bu, Y.; Li, H. Synthesis and modification of ultrathin g-C_3N_4 for photocatalytic energy and environmental applications. *Renew. Sustain. Energy Rev.* **2022**, *173*, 113110. [CrossRef]
29. Zhang, M.; Du, H.; Ji, J.; Li, F.; Lin, Y.C.; Qin, C.; Zhang, Z.; Shen, Y. Highly Efficient Ag_3PO_4/g-C_3N_4 Z-Scheme Photocatalyst for its Enhanced Photocatalytic Performance in Degradation of Rhodamine B and Phenol. *Molecules* **2021**, *26*, 2062. [CrossRef]
30. Zhou, C.; Cao, J.; Lin, H.; Xu, B.; Huang, B.; Chen, S. Controllable synthesis and photocatalytic activity of Ag/BiOI based on the morphology effect of BiOI substrate. *Surf. Coat. Technol.* **2015**, *272*, 213–220. [CrossRef]
31. Han, D.; Li, B.; Yang, S.; Wang, X.; Gao, W.; Si, Z.; Zuo, Q.; Li, Y.; Li, Y.; Duan, Q.J.N. Engineering charge transfer characteristics in hierarchical Cu_2S QDs@ ZnO Nanoneedles with p–n heterojunctions: Towards highly efficient and recyclable photocatalysts. *Nanomaterials* **2018**, *9*, 16. [CrossRef] [PubMed]
32. Huang, Y.; Zhang, X.; Zhang, K.; Lu, P.; Zhang, D. Facile fabrication of sandwich-like BiOI/AgI/g-C_3N_4 composites for efficient photocatalytic degradation of methyl orange and reduction of Cr(VI). *J. Nanoparticle Res.* **2018**, *20*, 328. [CrossRef]
33. Chang, C.; Zhu, L.; Wang, S.; Chu, X.; Yue, L. Novel Mesoporous Graphite Carbon Nitride/BiOI Heterojunction for Enhancing Photocatalytic Performance Under Visible-Light Irradiation. *ACS Appl. Mater. Interfaces* **2014**, *6*, 5083–5093. [CrossRef] [PubMed]
34. Liu, Z.; Xu, X.; Fang, J.; Zhu, X.; Chu, J.; Li, B. Microemulsion synthesis, characterization of bismuth oxyiodine/titanium dioxide hybrid nanoparticles with outstanding photocatalytic performance under visible light irradiation. *Appl. Surf. Sci.* **2012**, *258*, 3771–3778. [CrossRef]
35. Tian, N.; Zhang, Y.; Liu, C.; Yu, S.; Li, M.; Huang, H. g-C_3N_4/$Bi_4O_5I_2$ 2D–2D heterojunctional nanosheets with enhanced visible-light photocatalytic activity†. *RSC Adv.* **2016**, *6*, 10895–10903. [CrossRef]
36. Sun, B.-W.; Li, H.-J.; Yu, H.-y.; Qian, D.-J.; Chen, M. In situ synthesis of polymetallic Co-doped g-C_3N_4 photocatalyst with increased defect sites and superior charge carrier properties. *Carbon* **2017**, *117*, 1–11. [CrossRef]
37. Gholipour, M.R.; Béland, F.; Do, T.-O. Post-Calcined Carbon Nitride Nanosheets as an Efficient Photocatalyst for Hydrogen Production under Visible Light Irradiation. *ACS Sustain. Chem. Eng.* **2016**, *5*, 213–220. [CrossRef]
38. Che, H.; Liu, L.; Che, G.; Dong, H.; Liu, C.; Li, C. Control of energy band, layer structure and vacancy defect of graphitic carbon nitride by intercalated hydrogen bond effect of NO_3-toward improving photocatalytic performance. *Chem. Eng. J.* **2018**, *357*, 209–219. [CrossRef]
39. Wang, Y.; Wang, D.; Li, H.; Jiang, W.; Liu, C.; Che, G. A visible-light-driven 3D Z-scheme photocatalyst by loading BiOI nanosheets onto g-C_3N_4 microtubes for efficient degradation of tetracycline and p-chlorophenol. *J. Mater. Sci.* **2021**, *56*, 5555–5569. [CrossRef]
40. Bu, Y.; Xu, J.; Li, Y.; Liu, Q.; Zhang, X. Enhanced photocatalytic activity of BiOI under visible light irradiation by the modification of MoS_2. *RSC Adv.* **2017**, *7*, 42398–42406. [CrossRef]
41. Xia, P.; Cao, S.; Zhu, B.; Liu, M.; Shi, M.; Yu, J.; Zhang, Y. Designing a 0D/2D S-scheme heterojunction over polymeric carbon nitride for visible-light photocatalytic inactivation of bacteria. *Angew. Chem. Int. Ed. Engl.* **2020**, *59*, 5218–5225. [CrossRef] [PubMed]
42. Cheng, F.; Yan, J.; Zhou, C.; Chen, B.; Li, P.; Chen, Z.; Dong, X. An alkali treating strategy for the colloidization of graphitic carbon nitride and its excellent photocatalytic performance. *J. Colloid Interface Sci.* **2016**, *468*, 103–109. [CrossRef] [PubMed]

43. Hui, L.; Wangchen, H.; Tian, C.Z.; Like, O.; Shaojun, Y. Photocatalytic removal of tetracycline by a Z-scheme heterojunction of bismuth oxyiodide/exfoliated g-C_3N_4: Performance, mechanism, and degradation pathway. *Mater. Today Chem.* **2022**, *23*, 100729.
44. Feng, H.; Liang, L.; Liu, Y.; Huang, Z.; Li, L. Efficient nano-regional photocatalytic heterostructure design via the manipulation of reaction site self-quenching effect. *Appl. Catal. B Environ. Energy* **2018**, *243*, 220–228. [CrossRef]
45. Wei, Q.; Cheng, C.; Zhuoyun, T.; Dehua, X.; Dingren, M.; Yajing, H.; Qiyu, L.; Chun, H.; Dong, S.; Bin, H. Electron-rich/poor reaction sites enable ultrafast confining Fenton-like processes in facet-engineered BiOI membranes for water purification. *Appl. Catal. B Environ. Energy* **2021**, *304*, 120970.
46. Zhong, S.; Wang, B.; Zhou, H.; Li, C.; Peng, X.; Zhang, S. Fabrication and characterization of Ag/BiOI/GO composites with enhanced photocatalytic activity. *J. Alloys Compd.* **2019**, *806*, 401–409. [CrossRef]
47. Yu, C.; Yu, J.C.; Fan, C.; Wen, H.; Hu, S. Synthesis and characterization of Pt/BiOI nanoplate catalyst with enhanced activity under visible light irradiation. *Mater. Sci. Eng. B* **2009**, *166*, 213–219. [CrossRef]
48. Chang, C.; Zhu, L.; Fu, Y.; Chu, X. Highly active Bi/BiOI composite synthesized by one-step reaction and its capacity to degrade bisphenol A under simulated solar light irradiation. *Chem. Eng. J.* **2013**, *233*, 305–314. [CrossRef]
49. Feng, Z.; Zeng, L.; Zhang, Q.; Ge, S.; Zhao, X.; Lin, H.; He, Y. In situ preparation of g-C_3N_4/$Bi_4O_5I_2$ complex and its elevated photoactivity in Methyl Orange degradation under visible light. *J. Environ. Sci.* **2020**, *87*, 149–162. [CrossRef]
50. Li, H.; Wang, D.; Miao, C.; Xia, F.; Wang, Y.; Wang, Y.; Liu, C.; Che, G. g-C_3N_4/BiOI S-scheme heterojunction: A 2D/2D model platform for visible-light-driven photocatalytic CO_2 reduction and pollutant degradation. *J. Environ. Chem. Eng.* **2022**, *10*, 108201. [CrossRef]
51. Dong, G.; Wang, Y.; Lei, H.; Tian, G.; Qi, S.; Wu, D. Hierarchical mesoporous titania nanoshell encapsulated on polyimide nanofiber as flexible, highly reactive, energy saving and recyclable photocatalyst for water purification. *J. Clean. Prod.* **2020**, *253*, 120021. [CrossRef]
52. Shi, H.; Yu, Y.; Zhang, Y.; Feng, X.; Zhao, X.; Tan, H.; Khan, S.U.; Li, Y.; Wang, E. Polyoxometalate/TiO_2/Ag composite nanofibers with enhanced photocatalytic performance under visible light. *Appl. Catal. B Environ. Energy* **2017**, *221*, 280–289. [CrossRef]
53. Ong, W.-J.; Tan, L.-L.; Chai, S.-P.; Yong, S.-T.; Mohamed, A.R. Surface charge modification via protonation of graphitic carbon nitride (g-C_3N_4) for electrostatic self-assembly construction of 2D/2D reduced graphene oxide (rGO)/g-C_3N_4 nanostructures toward enhanced photocatalytic reduction of carbon dioxide to methane. *Nano Energy* **2015**, *13*, 757–770. [CrossRef]
54. Gong, Y.; Yu, H.; Chen, S.; Quan, X. Constructing metal-free polyimide/g-C_3N_4 with high photocatalytic activity under visible light irradiation. *RSC Adv.* **2015**, *5*, 83225–83231. [CrossRef]
55. Li, X.; Raza, S.; Liu, C. Directly electrospinning synthesized Z-scheme heterojunction TiO_2@Ag@Cu_2O nanofibers with enhanced photocatalytic degradation activity under solar light irradiation. *J. Environ. Chem. Eng.* **2021**, *9*, 106133.
56. Luna-Sanguino, G.; Ruíz-Delgado, A.; Duran-Valle, C.; Malato, S.; Faraldos, M.; Bahamonde, A. Impact of water matrix and oxidant agent on the solar assisted photodegradation of a complex mix of pesticides over titania-reduced graphene oxide nanocomposites. *Catal. Today* **2021**, *380*, 114–124. [CrossRef]
57. Nguyen, T.P.; Tran, Q.B.; Ly, Q.V.; Thanh Hai, L.; Le, D.T.; Tran, M.B.; Ho, T.T.T.; Nguyen, X.C.; Shokouhimehr, M.; Vo, D.-V.N.; et al. Enhanced Visible Photocatalytic Degradation of Diclofen over N-doped TiO_2 assisted with H_2O_2: A Kinetic and Pathway Study. *Arab. J. Chem.* **2020**, *13*, 8361–8371. [CrossRef]
58. Li, X.; Wang, B.; Shu, X.; Wang, D.; Xu, G.; Zhang, X.; Lv, J.; Wu, Y. An amorphous MoSx modified g-C_3N_4 composite for efficient photocatalytic hydrogen evolution under visible light†. *RSC Adv.* **2019**, *9*, 15900–15909. [CrossRef]
59. Chen, Y.; Huang, W.; He, D.; Situ, Y.; Huang, H. Construction of Heterostructured g-C_3N_4/Ag/TiO_2 Microspheres with Enhanced Photocatalysis Performance under Visible-Light Irradiation. *ACS Appl. Mater. Interfaces* **2014**, *6*, 14405–14414. [CrossRef]
60. Liu, J.; Li, Y.; Liu, X.; Fu, J.; Li, J.; Liu, Y.; Wang, H.; Li, S. Synthesis of a novel flower-like $Bi_4Ti_3O_{12}$/AgI Z-type heterojunction for efficient photocatalytic removal of tetracycline antibiotic and RhB. *J. Water Process Eng.* **2024**, *67*, 106262. [CrossRef]
61. Alsalme, A.; Hassan, M.M.; Eltawil, M.A.; Amin, A.E.; Soltan, A.; Messih, M.F.A.; Ahmed, M.A. Rational sonochemical engineering of Ag_2CrO_4/g-C_3N_4 heterojunction for eradicating Rh B dye under full broad spectrum. *Heliyon* **2024**, *10*, e31221. [CrossRef] [PubMed]
62. Wang, J.; Lin, W.; Dong, M.; Xing, Y.; Zhang, Q. Facile synthesize of CdS QDs decorated Bi_2MoO_6/$Bi_2Mo_3O_{12}$ heterojunction photocatalysts and enhanced performance of visible light removal of organic pollutants. *Environ. Technol.* **2020**, *42*, 3581–3594. [CrossRef] [PubMed]
63. Khan, A.; Altaf, M.; Shahid, M.; Zeyad, M.T. In situ solid-state fabrication of Z-Scheme $BiVO_4$/g-C_3N_4 heterojunction photocatalyst with highly efficient-light visible activity and their antibacterial properties against bacterial pathogens. *J. Mol. Struct.* **2023**, *1300*, 137222. [CrossRef]
64. Gao, M.; Li, W.; Su, X.; Li, Z.; Ding, X.; Du, X.; Ren, Y.; Zhang, H.; Feng, J.; Wei, T. A regenerable Cu_2O/BiOBr S-scheme heterojunction photocatalysts for efficient photocatalytic degradation of mixed organic pollutants. *Sep. Purif. Technol.* **2023**, *313*, 123447. [CrossRef]
65. Wang, M.; Li, C.; Liu, B.; Qin, W.; Xie, Y. Facile Synthesis of Nano-Flower β-Bi_2O_3/TiO_2 Heterojunction as Photocatalyst for Degradation Rh B. *Molecules* **2023**, *28*, 882. [CrossRef]
66. Gang, R.; Xu, L.; Xia, Y.; Cai, J.; Zhang, L.; Wang, S.; Li, R. Fabrication of MoS_2 QDs/ZnO nanosheet 0D/2D heterojunction photocatalysts for organic dyes and gaseous heavy metal removal. *J. Colloid Interface Sci.* **2020**, *579*, 853–861. [CrossRef]

67. Liu, Z.; Wang, N.; Wang, H.; Zhang, X.; Li, J.; Liu, X.; Duan, J.; Hou, B. Constructing S-scheme heterojunction of octahedral flower-like $ZnIn_2S_4/Bi_2WO_6$ nanocone with enhanced photocatalytic activity. *J. Electroanal. Chem.* **2022**, *915*, 116360.
68. Wu, Y.; Yin, Y.; Su, X.; Yi, G.; Oderinde, O.; Shi, S.; Zeng, H.; Xing, B.; Zhang, C.; Zhang, Y. Excellent performance of $BiOI/AgEuW_2O_8$ S-Scheme heterojunction for photocatalytic degradation of contaminants under visible light: Experimental and computational studies. *J. Phys. Chem. Solids* **2024**, *192*, 112092. [CrossRef]
69. Muhammad Khalid, H.; Khalid, N.R.; Muhammad, T.; Imen, K.; Hussein, A. Fabrication of CuO/MoO_3 p-n heterojunction for enhanced dyes degradation and hydrogen production from water splitting. *Int. J. Hydrog. Energy* **2021**, *47*, 15491–15504.
70. Yu, Y.; Chen, F.; Jin, X.; Min, J.; Duan, H.; Li, J.; Wu, Z.; Cao, B. Oxygen Vacancies-Rich S-Cheme BiOBr/CdS Heterojunction with Synergetic Effect for Highly Efficient Light Emitting Diode-Driven Pollutants Degradation. *Nanomaterials* **2023**, *13*, 830. [CrossRef]
71. Van, K.N.; Huu, H.T.; Nguyen Thi, V.N.; Le Thi, T.L.; Truong, D.H.; Truong, T.T.; Dao, N.N.; Vo, V.; Tran, D.L.; Vasseghian, Y. Facile construction of S-scheme $SnO_2/g\text{-}C_3N_4$ photocatalyst for improved photoactivity. *Chemosphere* **2021**, *289*, 133120. [CrossRef] [PubMed]
72. Cui, Y.; Lin, C.; Li, M.; Zhu, N.; Meng, J.; Zhao, J. $CuWO_4/CuS$ heterojunction photocatalyst for the application of visible-light-driven photodegradation of dye pollutions. *J. Alloys Compd.* **2021**, *893*, 162181. [CrossRef]
73. Zhu, L.; Luo, J.; Dong, G.; Lu, Y.; Lai, Y.; Liu, J.; Chen, G.; Zhang, Y. Enhanced photocatalytic degradation of organic contaminants over a $CuO/g\text{-}C_3N_4$ p–n heterojunction under visible light irradiation. *RSC Adv.* **2021**, *11*, 33373–33379. [CrossRef] [PubMed]
74. Shah, A.; Akhtar, S.; Mahmood, F.; Urooj, S.; Siddique, A.B.; Irfan, M.I.; Naeem-ul-Hassan, M.; Sher, M.; Alhoshani, A.; Rauf, A.; et al. Fagonia arabica extract-stabilized gold nanoparticles as a highly selective colorimetric nanoprobe for Cd^{2+} detection and as a potential photocatalytic and antibacterial agent. *Surf. Interfaces* **2024**, *51*, 104556. [CrossRef]